PHYSICAL REVIEW B VOLUME 44, NUMBER 21 1 DECEMBER 1991-I

Structural and magnetic properties of Er thin films and Er/Y superlattices. II. Modification of the commensurate spin states

J.A. Borchers* and M.B. Salamon
Department of Physics and Materials Research Laboratory, University of Illinois at Urbana-Champaign, 1110 West Green Street, Urbana, Illinois 61801

R.W. Erwin and J.J. Rhyne†
National Institute of Standards and Technology, Gaithersburg, Maryland 20899

G.J. Nieuwenhuys
Kamerlingh Onnes Laboratory, Leiden University, P.O. Box 9506, 2300 RA Leiden, The Netherlands

R.R. Du, C.P. Flynn, and R.S. Beach
Department of Physics and Materials Research Laboratory, University of Illinois at Urbana-Champaign, 1110 West Green Street, Urbana, Illinois 61801

(Received 19 April 1991; revised manuscript received 18 July 1991)

Continuing the analysis of epitaxial erbium thin films and Er/Y superlattices, we report the effects of basal-plane strain on the modulated spin structure as determined from bulk magnetization and neutron-diffraction measurements detailed in a previous paper [Phys. Rev. B **43**, 3123 (1991)]. The phase angle of the c-axis-modulated spin order is larger than that of bulk Er in even the thickest films and is virtually independent of temperature in the superlattices. The sequence and stability of c-axis commensurate states in bulk Er are altered in all samples considered. In the superlattices, the net moment state with four spins up followed by three spins down dominates the temperature and field phase diagram. An additional intermediate spin configuration with a net moment of half the saturation moment develops in the superlattice with the thinnest Er interlayers. A phenomenological calculation of the exchange integral demonstrates that epitaxial strain and lattice clamping can lead to an enhancement of the phase angle. Specifically, additional commensurate phases may arise due to strain-induced variations of the nearest-neighbor and next-nearest-neighbor spin interactions, as shown in the context of the axial-next-nearest-neighbor Ising model.

I. INTRODUCTION

In recent years, neutron and synchrotron-radiation diffraction studies of the rare-earth metals Ho,[1] Th,[2] and Er[3] have demonstrated that the spin structure in each material exhibits a series of states in which the modulation is commensurate with the lattice periodicity, and as a result the periodic spin order does not change smoothly with temperature. In the case of holmium, Gibbs *et al.*[1] explained the synchrotron results using a model in which pairs of ferromagnetic planes lie along successive basal plane axes to form a "bunched" spiral. Commensurate states form due to the development of "spin slips" (defined as a missing member of a pair along an easy direction) with increasing temperature. A similar synchrotron investigation of Ho/Y superlattices[4] searched for possible alteration or interruption of the spin-slip structures by artificial interfaces.

In this paper, Er thin films and Er/Y superlattices, described previously,[5–7] are used to probe the effects of epitaxy and artificial periodicity on commensurate c-axis structures. We show that changes observed in the nature and stability of erbium spin states follow from strain-induced modifications of the exchange interaction. The behavior is qualitatively consistent with predictions from the axial-next-nearest-neighbor Ising (ANNNI) model, developed to explain the spin commensurations in bulk Er.[8]

II. COMMENSURATE SPIN STATES IN BULK ERBIUM

Bulk erbium exhibits three distinct magnetic phases below 85 K: sinusoidal c-axis modulation (CAM) of the spin amplitude from 85 to 52 K, basal-plane spiral modulation and "squared" CAM from 52 to 20 K, and c-axis conical ferromagnetism below 20 K. Neutron diffraction studies[9] indicate that the CAM phase angle decreases from 51°/layer at T_N to 45°/layer at T_C. The spiral and CAM wavelengths match down to T_C; below T_C the spiral phase angle stabilizes at a value of 43°/layer. Figure 1(a) shows the phase angle for bulk Er as a function of temperature.[3] The commensurate states are labeled $2l/n$ where n is the number of c-axis layers in the mag-

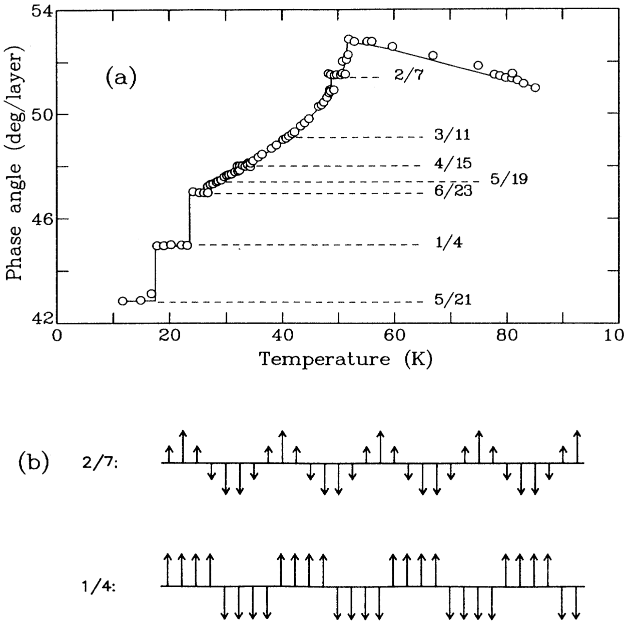

FIG. 1. (a) Temperature dependence of the phase angle of the Er CAM and basal plane spiral obtained from synchrotron measurements by Gibbs (Ref. 3). The intermediate states are labeled using the notation described in the text. (b) Schematic drawings of the $\frac{2}{7}$ and $\frac{1}{4}$ states. The spins are shown perpendicular to the modulation direction for clarity.

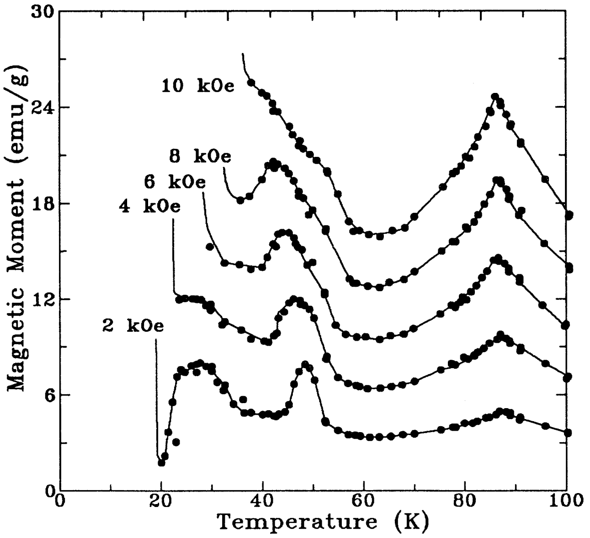

FIG. 2. Magnetization as a function of temperature for bulk Er in c-axis fields [Fig. 13 from Gray and Spedding (Ref. 10)]. The two anomalies above T_C correlate with the formation of the $\frac{6}{23}$ and $\frac{2}{7}$ net moment states observed by Gibbs (refer to Fig. 1).

netic unit cell and l is the number of 2π phase changes in that cell. The schematic representations of the $\frac{2}{7}$ and $\frac{1}{4}$ intermediate states in Fig. 1(b) show clearly that the $\frac{2}{7}$ state has a net magnetic moment equal to one-seventh the saturation moment, while the $\frac{1}{4}$ state has none. The $\frac{4}{15}$ and $\frac{6}{23}$ states have moments of $\frac{1}{15}M_{\mathrm{sat}}$ and $\frac{1}{23}M_{\mathrm{sat}}$, respectively.

The bulk Er magnetization data of Gray and Spedding[10] shown in Fig. 2 also reveal these "lock-in" states, although the origin of the anomalies was not appreciated at the time of the study. Extrapolation of the two prominent peak positions to the zero field gives transition temperatures of 28 and 50.5 K, respectively. These features mark the development of the $\frac{6}{23}$ and the $\frac{2}{7}$ net moment states observed by Gibbs.[3] The dip near 42 K may be associated with the $\frac{3}{11}$ state. Similar features are evident in susceptibility measurements for three Er/Y alloys[10] with Y concentrations ranging from 25 to 75 at. % but have very different onset temperatures.

It has been demonstrated[11,8] that competing exchange interactions of neighboring lattice planes give rise to a discrete sequence of commensurate states, similar to those observed in bulk Er and its alloys. The application of the three-plane interaction model and ANNNI model to bulk Er and to the epitaxial structures is described in Sec. VI.

III. EXPERIMENTAL PROCEDURES

In this paper we consider a series of Er films and superlattices grown by Molecular Beam Epitaxy at the University of Illinois on 1.2-cm^2 sapphire substrates covered with $\approx$1000 Å of Nb and 300–500 Å of yttrium. Details of the growth and structural characterization have been provided in a previous paper (paper I).[5] Here we focus on the formation of intermediate spin states in seven thin films with Er thicknesses ranging from 375 to 14 500 Å and in four superlattices, $[\mathrm{Er}_{31.5}\,|\mathrm{Y}_{21}]_{60}$, $[\mathrm{Er}_{25.5}\,|\mathrm{Y}_{25.5}]_{80}$, $[\mathrm{Er}_{23.5}\,|\mathrm{Y}_{19}]_{100}$, and $[\mathrm{Er}_{13.5}\,|\mathrm{Y}_{25}]_{100}$,[12] as revealed by magnetization and neutron scattering data.

Neutron scattering experiments[5] were performed at the National Institute of Standards and Technology on a triple axis spectrometer. In addition to zero field K_z scans through the $(10\bar{1}0)$ and (0002) reflections, a series of $[1\bar{2}1l]$ scans were carried out in c-axis fields up to 50 kG. Due to the vertical field geometry of the NbTi superconducting magnet, it was necessary to orient the growth plane parallel to the scattering plane. To perform the scans the entire magnet and Dewar assembly was rotated ±7° about a horizontal axis. Due to limited vertical collimation, the resolution was approximately 0.05 Å^{-1} compared with 0.02 Å^{-1} for the $[000l]$ scans.

The phase angles of the spin modulation, the moments, and the transition temperatures were determined from the positions and intensities of the magnetic reflections. The CAM magnetic structure gives rise to peaks displaced from the nuclear basal plane reflections by $\Delta K_z = \pm Q$, where Q is the CAM wave vector. Higher order magnetic reflections develop as the CAM "squares-up." The basal plane helix leads to similar magnetic

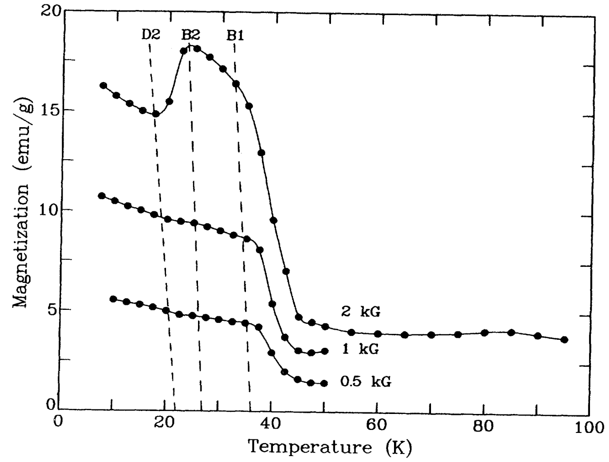

FIG. 3. Field-cooled magnetization vs temperature for the 860-Å Er film in 2-, 1-, and 0.5-kG *c*-axis fields. The feature near 85 K marks $T_{N\parallel}$. The anomalies are designated by $B1$ and $B2$ for the maxima and $D2$ for the depression.

reflections about the *c*-axis structural peaks. In superlattice samples, both magnetic and structural reflections are surrounded by superlattice sidebands. The relative phase and moment of each atomic plane can be extracted from fits of the neutron data to the damped rectangle-wave model described in paper I.

IV. ER THIN FILMS

A. Magnetic moment and transition temperatures

Susceptibility data for the Er films are typified by Fig. 3, which shows the temperature-dependent magnetization for the 860-Å film. The anomaly near 85 K marks the *c*-axis Néel temperature $T_{N\parallel}$. The effective moment μ_{expt} was extracted from fits of the magnetization above $T_{N\parallel}$ to the Curie-Weiss law. The moments are given in Table I and, except for the 860- and 14 500-Å films, agree with the Er magnetization value of $9.6\mu_B$.

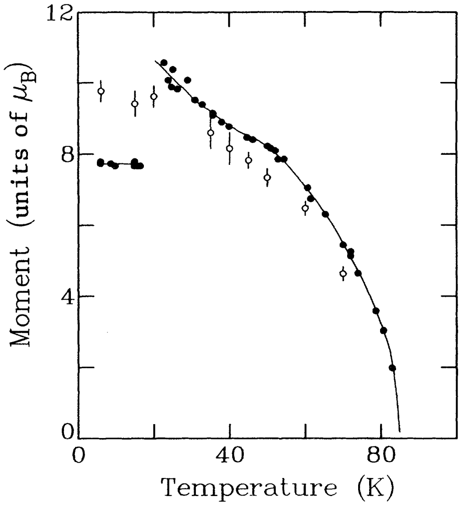

FIG. 4. The *c*-axis moment (open circles) as a function of temperature for the 860-Å film. The $\mu_{\parallel}^{(1)}$ values were calculated from the intensities of the $(11\bar{2}0)^{\pm}$ magnetic peaks relative to the nuclear reflection. Data for bulk Er (Ref. 9) (solid line and solid circles) are shown for comparison.

The values for $T_{N\parallel}$ in Table I were obtained by extrapolating the position of the high temperature cusp to zero field. These results tend to decrease as the basal plane strain, also listed in Table I, increases. $T_{N\perp}$, which marks the development of the basal plane spiral, was approximated from the temperature dependence of the $(0002)^{\pm}$ neutron reflections. The 860- and 1750-Å films have transition temperatures near 40–45 K while $T_{N\perp} \approx 49$ K for the 9500-Å sample; the bulk value is 52 K.

For each film, the *c*-axis moment per Er atom was calculated as a function of temperature from the intensities of the $(10\bar{1}0)^{\pm}$ or $(11\bar{2}0)^{\pm}$ and higher-order magnetic peaks. The amplitude of the fundamental peak for the 860-Å film is plotted versus temperature in Fig. 4 along with that for bulk Er;[9] the shift in $T_{N\parallel}$ is readily apparent. Higher-order magnetic reflections were not observed for this film, but third-order satellites of the $(10\bar{1}1)^{-}$ and

TABLE I. The *c*-axis Néel temperatures and experimental saturation moments for the Er thin films were determined from bulk magnetization measurements. The first and third components of the CAM moment $\mu_{\parallel}^{(1)}, \mu_{\parallel}^{(3)}$ and the basal plane moments $\mu_{\perp}$ were extracted from magnetic peak intensities at 10 K. They are compared to bulk Er values measured above T_C (Ref. 9). The basal plane strain values at 10 K were tabulated in paper I and are repeated here for reference.

Er thick	ϵ_{xx}	Bulk mag		Neutron		
(Å)	(10^{-3})	$T_{N\parallel}$ (K)	μ_{expt}/μ_B	$\mu_{\parallel}^{(1)}/\mu_B$	$\mu_{\parallel}^{(3)}/\mu_B$	$\mu_{\perp}/\mu_B$
375		83.8 ± 0.35	10.2 ± 0.6			
860	6.77	84.2 ± 0.40	12.3 ± 1.6	9.8 ± 0.3		3.1 ± 0.1
1750	5.96	84.5 ± 0.30	9.8 ± 0.4	10.5 ± 0.2	2.6 ± 0.1	3.1 ± 0.2
3900		84.3 ± 0.30	10.4 ± 0.5			
3950	−0.703	84.7 ± 0.25	9.6 ± 0.4	10.2 ± 0.2	2.0 ± 0.2	3.5 ± 0.2
9500	−0.453	85.6 ± 0.40	10.0 ± 0.4	10.2 ± 0.8		3.4 ± 0.2
14500		85.2 ± 0.30	10.9 ± 0.4			
Bulk Er		85	9.6	10.5	2.4	3.8

$(10\bar{1}\bar{1})^+$ peaks were detected below 35 K for the 3950- and 1750-Å films. The amplitudes of the first and third harmonics at 10 K are given in Table I. For the 9500-Å film the $\mu_{\parallel}^{(1)}$ value is merely an estimate because the squared spin structure locks-in to the $\frac{1}{4}$ commensurate state, superposing the first- and third-order magnetic reflections. The basal plane moment that develops below $T_{N\perp}$ was calculated from the intensities of the $(0002)^{\pm}$ peaks. The 10-K values are listed in Table I. The total moments for the thin films were calculated by squaring $\mu_{\perp}$ with the amplitude of the c-axis modulation and are $9.2\mu_B$ for the 1750-Å film and $9.3\mu_B$ for the 3950-Å film at 10 K. These values differ from the $9.0\mu_B$ Er moment[9] primarily because higher-order Fourier components have not been measured.

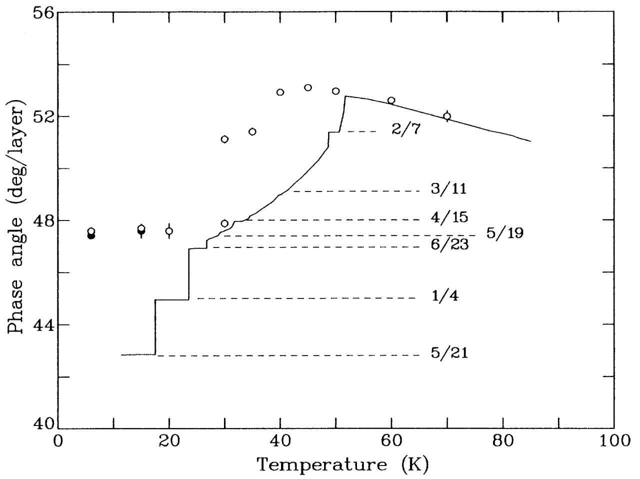

FIG. 5. Phase angle plotted vs temperature for the 860-Å Er film. The solid circles mark the turn angles for the basal plane spiral obtained from the positions of the $(0002)^{\pm}$ satellites. The open circles correspond to the phase angles of the CAM extracted from the positions of the $(11\bar{2}0)^{\pm}$ magnetic reflections. The phase angle of the CAM in bulk Er (solid line) (Ref. 3) is shown for comparison.

B. Intermediate spin states

Neutron diffraction and magnetization results indicate that the spin structures of the epitaxial films change via a sequence of commensurate states as does bulk Er, but the stability of these states depends on film thickness. For example, the magnetization data for the 860-Å film in Fig. 3 show no evidence of a first-order ferromagnetic transition; rather the curves exhibit distinct anomalies similar to those of bulk Er (Fig. 2). For the 860-Å film, the 2-kG curve has a pronounced "bump" ($B2$) and a "dip" ($D2$), while the 1-kG and 0.5-kG curves show two less distinct maxima ($B1$ and $B2$) in addition to a depression ($D2$). Extrapolation to zero field gives $T_{B1} = 36.0 \pm 2.0$ K, $T_{B2} = 27.0 \pm 2.0$ K, and $T_{D2} = 22.0 \pm 1.5$ K.

The phase angles of the CAM and basal plane spiral for the 860-Å film are plotted versus temperature in Fig. 5. As in bulk, the spiral and CAM angles are equal and vary discontinuously with temperature. At each temperature, however, the angles are larger than the bulk Er values. Below 20 K, the turn angle stabilizes near 47.6°/layer, close to the 47.4°/layer phase angle for the $\frac{5}{19}$ state. We associate this commensurate state, which has no net moment, with the depression $D2$ in the susceptibility. The presence of two distinct $(11\bar{2}0)^+$ reflections in the 30-K neutron data indicates that two spin states with phase angles close to the $\frac{4}{15}$ and $\frac{2}{7}$ commensurate structures coexist. We identify T_{B2} with the development of the $\frac{4}{15}$ net moment state. Finally the phase angle of 51.4°/layer at 35 K indicates that T_{B1} characterizes the formation of the $\frac{2}{7}$ net moment state.

Susceptibility curves for the 1750- and 3900-Å Er films are similar to the data in Fig. 3. Anomalies are evident at the same temperatures (within experimental error) as those for the 860-Å film. Diffraction measurements for the 1750-Å film confirm that the associated "lock-in" structures are identical to those identified for the 860-Å sample.

The magnetization data for the 9500-Å film differ substantially from the thinner films; the anomalies are more pronounced (Fig. 6). The characteristic temperatures of these features are $T_{B1} = 47.0 \pm 1.0$ K, $T_{D1} = 35.2 \pm 1.0$ K, $T_{B3} = 25.5 \pm 1.5$ K, and $T_{D3} = 16.0 \pm 1.0$ K. The 2-kG and zero-field turn angles of the CAM and the zero-field phase angle of the basal plane spiral are plotted as a function of temperature in Fig. 7. Both data sets suggest that the maximum marked $B1$ correlates with the development of the $\frac{2}{7}$ net moment state. The 2-kG turn angle of 49.4°/layer at 32.5 K identifies the depression $D1$ with the $\frac{3}{11}$ structure. The bump $B3$ may be associated with the development of the $\frac{4}{15}$ net moment state, though the phase angles measured near 25 K are slightly

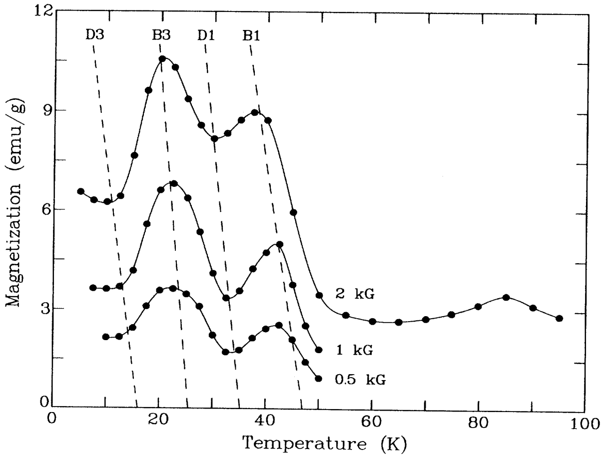

FIG. 6. Field-cooled magnetization vs temperature for the 9500-Å Er film in 2-, 1-, and 0.5-kG fields applied along the c axis. The anomalies are designated by $B1$ and $B3$ for the maxima and $D1$ and $D3$ for the depressions.

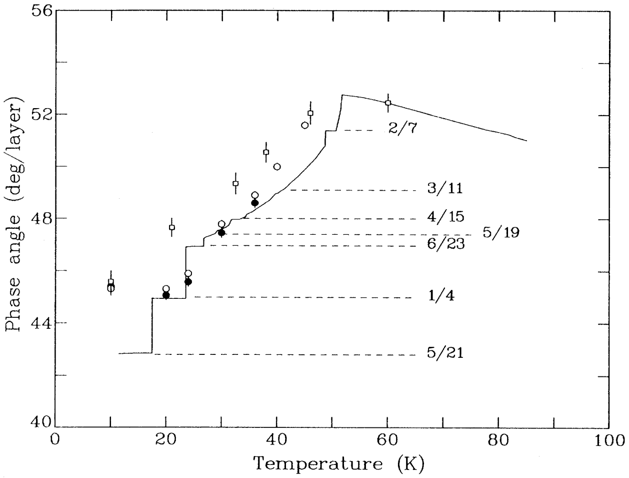

FIG. 7. Phase angle as a function of temperature for the 9500-Å Er film. The turn angles for the basal plane spiral calculated from the positions of the $(0002)^{\pm}$ satellites are marked by solid circles. The CAM turn angles obtained from the positions of the $(10\bar{1}0)^{\pm}$ reflections in zero field are designated by open circles and the phase angles from the positions of the $(11\bar{2}0)^{\pm}$ peaks in a 2-kG field are marked by squares. The phase angle of the CAM in bulk Er (Ref. 3) (solid line) is shown for comparison.

smaller than 48.0°/layer. We note that the 47.0°/layer turn angle expected for the $\frac{6}{23}$ net moment state is not observed. The phase angle data clearly indicate that the CAM locks in to the $\frac{1}{4}$ spin structure below 20 K, giving rise to the low-temperature depression $D3$ in Fig. 6. The features of the susceptibility data for the 14 500-Å film are similar in appearance to those of the 9500-Å film data, though less pronounced and at slightly lower temperatures.

As may be expected, the temperature-dependent spin structures of the thicker films more closely resemble those of bulk Er than do those of the strained thin films. This observation is supported by data for the 3950-Å film whose magnetization curve has only a single anomaly near $T = 47.0 \pm 2.0$ K. Phase angle measurements confirm that this feature marks the formation of the $\frac{2}{7}$ net moment state at a characteristic temperature closer to T_{B1} values for the 9500-Å film and bulk than to values for the thinner films. This result follows, we believe, from the reduced epitaxial strain for that film relative to the others (refer to Table I).

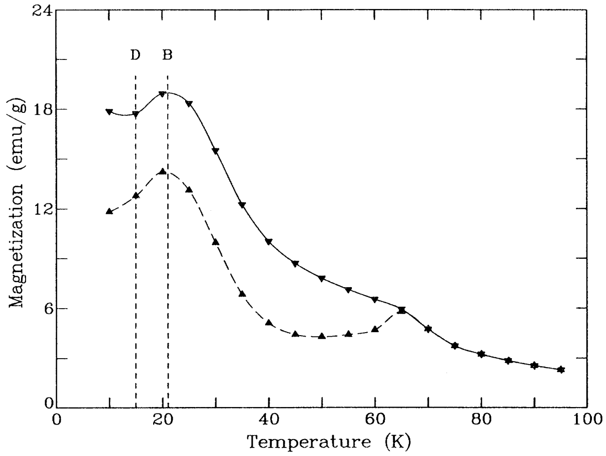

FIG. 8. The field-cooled (solid line) and zero-field-cooled (dashed line) magnetization of $[\mathrm{Er}_{13.5}|\mathrm{Y}_{25}]_{100}$ in a 2-kG field applied along the c axis. The high-temperature feature marks $T_{N\parallel} = 67.8$ K.

V. ER/Y SUPERLATTICES

A. Magnetic moment and transition temperatures

Magnetization measurements and neutron diffraction scans performed in c-axis fields on the four Er/Y superlattices give substantially different results from those of the thin films and bulk Er. Figure 8 shows the field-cooled and zero-field-cooled magnetization versus temperature for $[\mathrm{Er}_{13.5}|\mathrm{Y}_{25}]_{100}$ in a 2-kG c-axis field. Fits of the susceptibility above $T_{N\parallel}$ to the Curie-Weiss law give saturation moment values that are comparable to bulk. These parameters are listed in Table II.

The c-axis Néel temperatures, from both neutron diffraction measurements of the $(10\bar{1}0)^{\pm}$ and $(10\bar{1}1)^{\pm}$ peak intensities and magnetization data, are reduced significantly from the bulk Er value of 85 K. Comparison with the a-axis lattice strain in Table II suggests that $T_{N\parallel}$ for both the films and superlattices decreases as the epitaxial strain increases. The basal plane Néel temperature $T_{N\perp}$ is best determined from the $(0002)^{\pm}$ peak intensities. The resultant temperatures are listed in Table II; all are ***significantly*** lower than the bulk value of 52 K and the Er thin film values which range from 40 to 45 K.

TABLE II. μ_{expt} for the superlattices was extracted from fits of the magnetic susceptibility above $T_{N\parallel}$ to the Curie-Weiss law. The Néel temperatures, $T_{N\parallel}$ and $T_{N\perp}$, were extracted from the c- and a-axis susceptibility data, respectively, and from measurements of the magnetic neutron peak intensities. The basal plane strain values at 10 K were tabulated in paper I and are repeated here for reference.

Superlattice sample	ϵ_{xx} (10^{-3})	$\mu_{\mathrm{expt}}/\mu_B$	$T_{N\parallel}$ (K)		$T_{N\perp}$ (K)	
			Mag	Neut	Mag	Neut
$[\mathrm{Er}_{31.5}|\mathrm{Y}_{21}]_{60}$	12.95	10.6 ± 0.4	77.2 ± 0.5	80 ± 5	28 ± 2	30 ± 5
$[\mathrm{Er}_{23.5}|\mathrm{Y}_{19}]_{100}$	11.43	10.1 ± 0.3	74.9 ± 1.0	78 ± 1	28 ± 2	28.5 ± 0.5
$[\mathrm{Er}_{25.5}|\mathrm{Y}_{25.5}]_{80}$	—	10.1 ± 0.3	74.5 ± 1.0			
$[\mathrm{Er}_{13.5}|\mathrm{Y}_{25}]_{100}$	11.43	9.9 ± 0.5	67.8 ± 1.0	70 ± 5		30 ± 5

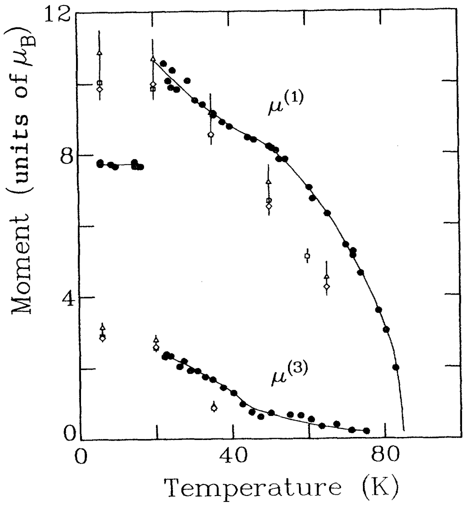

FIG. 9. The first- and third-order c-axis moments ($\mu_{\parallel}^{(1)}$ and $\mu_{\parallel}^{(3)}$, respectively) are plotted as a function of temperature for $[\mathrm{Er}_{23.5}|\mathrm{Y}_{19}]_{100}$ (diamonds), $[\mathrm{Er}_{13.5}|\mathrm{Y}_{25}]_{100}$ (squares), and $[\mathrm{Er}_{31.5}|\mathrm{Y}_{21}]_{60}$ (triangles). These moment values were extracted from fits of the $[10\bar{1}l]$ neutron diffraction scans to the damped rectangle-wave model. Data for bulk Er (Ref. 9) (solid lines and solid circles) are shown for comparison.

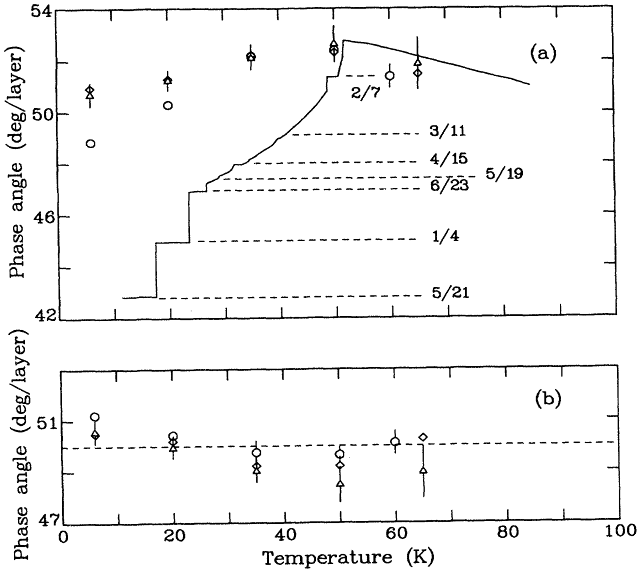

FIG. 10. (a) The phase angle/layer of the CAM in the Er portion of each bilayer is plotted vs temperature for $[\mathrm{Er}_{13.5}|\mathrm{Y}_{25}]_{100}$ (circles), $[\mathrm{Er}_{23.5}|\mathrm{Y}_{19}]_{100}$ (diamonds), and $[\mathrm{Er}_{31.5}|\mathrm{Y}_{21}]_{60}$ (triangles). These turn angles were extracted from fits of the $[10\bar{1}l]$ neutron scans to the damped rectangle-wave model. The turn angle for bulk Er (Ref. 3) (solid line) is shown for comparison. (b) The effective phase angle/layer of the CAM in the Y portion of each bilayer is plotted vs temperature for the same three superlattices. The dashed line marks the 50°/layer turn angle for bulk Y determined from neutron studies of dilute RE/Y alloys (Ref. 14).

The c-axis moment per Er atom for $[\mathrm{Er}_{13.5}|\mathrm{Y}_{25}]_{100}$, $[\mathrm{Er}_{23.5}|\mathrm{Y}_{19}]_{100}$, and $[\mathrm{Er}_{31.5}|\mathrm{Y}_{21}]_{60}$ was extracted from fits of the $[10\bar{1}l]$ neutron scans to the damped rectangle-wave model.[5] The amplitudes of the first- and third-order harmonics, $\mu_{\parallel}^{(1)}$ and $\mu_{\parallel}^{(3)}$, are plotted versus temperature in Fig. 9 along with bulk values.[9] The basal plane moments were obtained similarly from fits of the $[000l]$ scans. Near 10 K, $\mu_{\perp}$ for $[\mathrm{Er}_{13.5}|\mathrm{Y}_{25}]_{100}$, $[\mathrm{Er}_{23.5}|\mathrm{Y}_{19}]_{100}$, and $[\mathrm{Er}_{31.5}|\mathrm{Y}_{21}]_{60}$ is $2.8 \pm 0.4\mu_B$ and decreases rapidly with increasing temperature as expected from the reduced $T_{N\perp}$. The total saturation moments, calculated from the low-temperature basal plane moments and the amplitude of the c-axis square-wave modulation, are $9.1\mu_B$ for $[\mathrm{Er}_{31.5}|\mathrm{Y}_{21}]_{60}$, $8.5\mu_B$ for $[\mathrm{Er}_{23.5}|\mathrm{Y}_{19}]_{100}$, and $8.6\mu_B$ for $[\mathrm{Er}_{13.5}|\mathrm{Y}_{25}]_{100}$. These values are reasonably close to the 9.0 μ_B bulk moment.[9]

B. Phase angle of the periodic magnetic structure

Like the thin films, the Er/Y superlattices do not cascade through the full sequence of bulk commensurate states as the temperature is lowered. Because the susceptibility curves, typified by Fig. 8, show no pronounced features, we identify the zero field "lock-in" states from the phase angle data. The CAM phase advance in each layer of the superlattice was determined by fitting the neutron data to the damped rectangle-wave model.[5] The average CAM angle in the Er portion of each bilayer (ω_{Er}) is plotted versus temperature in Fig. 10(a) along with the bulk Er values.[3] Below 50 K this angle is significantly larger than bulk and decreases only slightly ($\leq 1°$) as the temperature is lowered. At low temperatures ω_{Er} for the superlattices approaches the 51.4°/layer angle of the $\frac{2}{7}$ commensurate state. The only exception is $[\mathrm{Er}_{13.5}|\mathrm{Y}_{25}]_{100}$ (circles) for which ω_{Er} decreases through the $\frac{2}{7}$ value to that of the $\frac{3}{11}$ state at 10 K. In the susceptibility data for this sample (Fig. 8), the onset of the $\frac{2}{7}$ net moment state is marked by a broad maximum near 25 K. The depression that follows at 20 K is related to the formation of the $\frac{3}{11}$ spin structure which has no net moment.

The effective phase of the CAM in the Y interlayers is plotted as a function of temperature in Fig. 10(b). Within the uncertainties of the fit, it is constant at 50°/layer. This value is reasonably close to the 51°/layer effective Y angle determined for Dy/Y superlattices[13] and is identical to the 50°/layer turn angle of the magnetic order in dilute rare-earth–yttrium alloys.[14] Significantly, the total phase shift of the CAM across the Y layers is not an integral multiple of π; the coupling is not simply ferro- or antiferromagnetic.

Determination of the phase angle of the basal plane spiral from $[000l]$ neutron scans near (0002) was less accurate because the basal plane moment is small relative to the c-axis moment, and the spiral magnetic peaks are broader than the CAM reflections. The calculated spiral angles were consistently lower than those of the CAM at the same temperatures, while the effective Y turn angles varied by as much as 3° from the 50°/layer value. In contrast, the Er spiral angle for $[\mathrm{Er}_{13.5}|\mathrm{Y}_{25}]_{100}$ extracted from low-angle measurements around the $(0000)^{\pm}$ reflections at 6 K was 2° *larger* than the corresponding CAM angle. We cannot rule out the possibility that the phase angle of the spiral and that of the CAM differ at low temperatures.

C. Field dependence of the spin structure

The effect of a c-axis field on the intermediate spin states identified in the previous section was also explored using neutron and magnetization techniques. Figure 11 shows the magnetization curves for $[\mathrm{Er}_{13.5}|\mathrm{Y}_{25}]_{100}$ at temperatures ranging from 10 to 60 K. (The c-axis field values have been corrected for demagnetization effects.[5]) Although these curves are markedly different from bulk Er data in many respects (i.e., the enhanced critical fields[5]), the most unusual features are the two plateaus. In low fields the 10-K isotherm levels off near 30 emu/g, a value which is approximately one-seventh of the total saturation moment. Similar features are evident in data for the other superlattices (such as $[\mathrm{Er}_{23.5}|\mathrm{Y}_{19}]_{100}$ (Ref. 5)). Further, the 20- to 50-K isotherms for $[\mathrm{Er}_{13.5}|\mathrm{Y}_{25}]_{100}$ reveal a second step at internal fields between 17 and 30 kOe. This plateau marks the development of an intermediate state with approximately one-half of the spins aligned (i.e., $M \approx 95$ emu/g in comparison to $M_{\mathrm{sat}} = 182$ emu/g at 40 K). Hysteresis measurements[15] indicate that this state also develops in $[\mathrm{Er}_{23.5}|\mathrm{Y}_{19}]_{100}$ at $T \approx 40$ K upon lowering the magnetic field. This spin structure is not evident in hysteresis data for the two superlattices with the thickest Er interlayers, $[\mathrm{Er}_{31.5}|\mathrm{Y}_{21}]_{60}$ and $[\mathrm{Er}_{25.5}|\mathrm{Y}_{25.5}]_{80}$.

To explore the origin of the two plateaus, $[11\bar{2}l]$ neutron scans were performed on $[\mathrm{Er}_{13.5}|\mathrm{Y}_{25}]_{100}$ as a function of the c-axis applied field. Two of the 10-K scans are shown in Fig. 12(a). (The magnetic peaks are broad due to the limited instrumental resolution in this scattering geometry.) While the positions of the central magnetic reflections are independent of field, the relative amplitudes of the superlattice harmonics shift slightly as the field is increased. Fits of these data to the damped rectangle-wave model suggest that the CAM phase angle in the Er portion of the bilayer changes from 50.3°/layer in zero field to 51.4°/layer in 10-kG applied fields (8.5 kOe internal field). The latter phase angle matches that of the $\frac{2}{7}$ commensurate spin state in bulk Er; the low field step in the magnetization thus marks the formation of the $\frac{2}{7}$ structure.

Similar diffraction scans for $[\mathrm{Er}_{13.5}|\mathrm{Y}_{25}]_{100}$ at 40 K are shown in Fig. 12(b). At this temperature, the CAM locks-in to the $\frac{2}{7}$ state between zero and 10 kG. At 27 kG (23 kOe internal field), the magnetic peaks shift toward the $(11\bar{2}0)$ structural reflection, and ferromagnetic scattering develops at the Bragg and superlattice sideband positions [i.e., as "wings" on the central reflection in Fig. 12(b)]. The ferromagnetic moment calculated from the intensities is about half of the Er moment at 40 K (refer to Fig. 9) in good agreement with the relative moment estimated from the magnetization data (Fig. 11).

To identify this spin structure, the structure factors of various moment configurations were calculated[6] and compared to the 27-kG neutron data. We assume that the spins are modulated along the c axis in an offset wave pattern with N_1 spins up followed by N_2 down, N_3 up, and N_4 down ($N_T = N_1 + N_2 + N_3 + N_4$). The magnetic moment in the superlattices is described by the following:

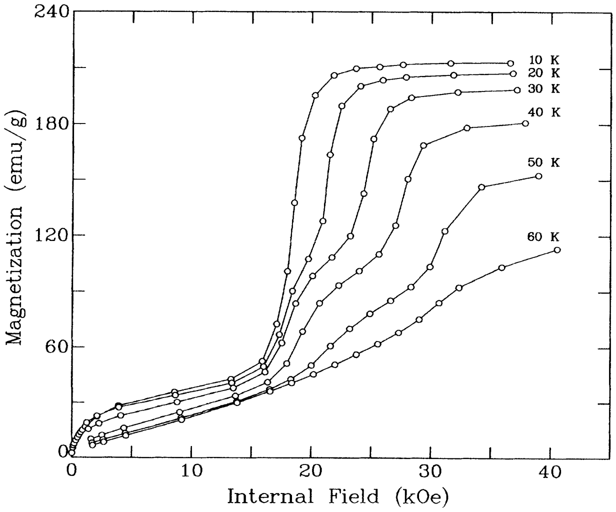

FIG. 11. Field dependence of the magnetization for $[\mathrm{Er}_{13.5}|\mathrm{Y}_{25}]_{100}$ at various temperatures. The c-axis fields have been corrected for demagnetization effects (Ref. 5).

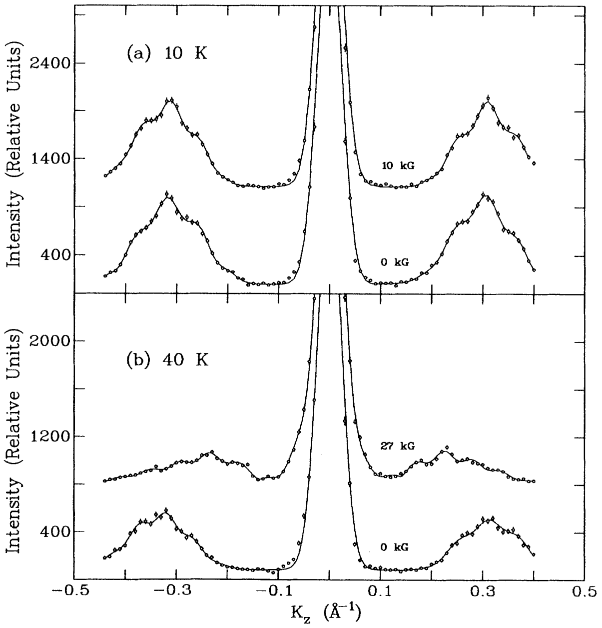

FIG. 12. (a) Neutron diffraction scans for $[\mathrm{Er}_{13.5}|\mathrm{Y}_{25}]_{100}$ along the $[11\bar{2}l]$ direction at 10 K in c-axis applied fields of 0 and 10 kG. (b) Neutron scans for $[\mathrm{Er}_{13.5}|\mathrm{Y}_{25}]_{100}$ along the $[11\bar{2}l]$ direction at 40 K in c-axis applied fields of 0 and 27 kG.

$$\langle \mathbf{S}_z(j,\xi)\rangle = C_A(j,\alpha)\langle S_z^A\rangle \Bigg\{ \frac{N_1 - N_2 + N_3 - N_4}{N_T} + \sum_{j=1}^{\infty} \frac{2e^{-\xi(j-1)}}{j\pi}\Bigg[\sin\left(\frac{j\phi_j}{2}\right) - \sin\left(\frac{j\phi_j}{2} - 2\pi j\frac{N_1}{N_T}\right) + \sin\left(\frac{j\phi_j}{2} - 2\pi j\frac{N_1+N_2}{N_T}\right) - \sin\left(\frac{j\phi_j}{2} - 2\pi j\frac{N_1+N_2+N_3}{N_T}\right)\Bigg]\Bigg\}\hat{\mathbf{z}}, \qquad (1)$$

where ξ is a damping factor. The total phase shift ϕ_j at the jth layer and the Er concentration $C_A(j,\alpha)$ are parameters defined in the damped rectangle-wave model.[5,13] The structural parameters used for these calculations were extracted from fits of the 35-K $[10\bar{1}l]$ scan for $[\mathrm{Er}_{13.5}|\mathrm{Y}_{25}]_{100}$ to this model. The "best guess" spin state has $N_1 = 7$, $N_2 = 3$, $N_3 = 8$, and $N_4 = 3$ down with $\xi = 0.1$. It follows geometrically from the $\frac{2}{7}$ state by flipping three sets of three spins. The state has a net moment of 0.42 $\langle S_z^A\rangle$, which is reasonably close to the experimental value. An exact comparison of the diffraction data to the model calculation is difficult, however, due to the poor resolution of the c-axis field scans. Similar spin states, such as $N_1 = N_3 = 8$ and $N_2 = N_4 = 3$, cannot be ruled out.

VI. ANALYSIS

In the simplest conventional model, the spin structures in bulk erbium result from competing ferromagnetic and antiferromagnetic spin interactions. In this section models for the exchange interaction in the rare earths are reviewed with emphasis on the ANNNI model, which specifically predicts the formation of "lock-in" states. It is shown that the modified magnetic behavior of the Er thin films and Er/Y superlattices can be qualitatively attributed to strain-induced changes of the exchange resulting from epitaxial growth.

A. Exchange interaction

In general the exchange Hamiltonian has the following form:

$$\mathcal{H}_{\mathrm{ex}} = -\sum_{i\neq j} \mathcal{J}(\mathbf{R}_i - \mathbf{R}_j)\mathbf{J}_i \cdot \mathbf{J}_j\,, \qquad (2)$$

where $\mathcal{J}(\mathbf{R}_i - \mathbf{R}_j)$ describes the long-range RKKY-like interaction between the ith and jth spins. The wavelength of the periodic magnetic structure is determined by the wave vector $\mathbf{Q}$, which maximizes the Fourier transform $\mathcal{J}(\mathbf{q})$. The simplest $\mathcal{J}(\mathbf{q})$ arises from the three-plane interaction model developed by Enz.[11] If all the spins in a given plane are parallel, the simplified exchange is written

$$\mathcal{J}(\mathbf{q}) = 4\mathcal{J}_0 + 2\mathcal{J}_1\cos(qd) + 2\mathcal{J}_2\cos(2qd), \qquad (3)$$

where $\mathcal{J}_0$ describes the interaction between the spins within a single plane, $\mathcal{J}_1$ is the interaction between the spins in neighboring planes, $\mathcal{J}_2$ is the interaction between next-nearest neighboring planes, and d is the interplanar distance. Maximizing Eq. (3) with respect to q at T_N gives

$$-\frac{\mathcal{J}_1}{4\mathcal{J}_2} = \cos(Q_N d)_{\mathrm{CAM}} \equiv \cos\omega_N\,. \qquad (4)$$

Periodic order is stable when $|\,\mathcal{J}_1\,| < 4\,|\,\mathcal{J}_2\,|$ and $\mathcal{J}_2 < 0$.

We assert that the primary source of temperature and strain dependence of the phase angle ω is the magnetoelastic energy. The total energy for bulk Er (excluding anisotropy) is

$$E = -\sigma^2 J^2 \sin^2\theta[4\mathcal{J}_0 + 2\mathcal{J}_1\cos\omega_{\mathrm{sp}} + 2\mathcal{J}_2\cos(2\omega_{\mathrm{sp}})] -\sigma^2 J^2\cos^2\theta[4\mathcal{J}_0 + 2\mathcal{J}_1\cos\omega_{\mathrm{CAM}} + 2\mathcal{J}_2\cos(2\omega_{\mathrm{CAM}})] + \tfrac{1}{2}\sum_{i,j} c_{ij}\epsilon_{ii}\epsilon_{jj} - \sum_j K_j\epsilon_{jj}\,, \qquad (5)$$

where ω_{sp} and ω_{CAM} are the turn angles of the spiral and CAM, respectively, c_{ij} are the elastic coefficients, ϵ_{ii} are the anomalous strains, and σ is the relative moment. The magnetoelastic coefficients K_j can be written as explicit functions of the turn angles and the cone angle θ:[16,17]

$$K_x = K_y = \tfrac{1}{2}(\,K_0^{x,y} + K_1^{x,y}\sin^2\theta\cos\omega_{\mathrm{sp}} + K_2^{x,y}\cos^2\theta\cos\omega_{\mathrm{CAM}}) \qquad (6)$$

$$K_z = K_0^z + K_1^z\sin^2\theta\cos\omega_{\mathrm{sp}} + K_2^z\cos^2\theta\cos\omega_{\mathrm{CAM}}\,.$$

Note that the effects of the CAM squaring at low temperatures can be included by replacing $\cos\omega_{\mathrm{CAM}}$ in Eqs. (5) and (6) with

$$\frac{1}{N_{SQ}}\sum_{m=0}^{\infty}\left(\frac{e^{-(2m+1)\delta}}{2m+1}\right)^2 \cos[(2m+1)\omega_{\mathrm{CAM}}], \qquad (7)$$

where the normalization factor N_{SQ} equals $\sum_{m=0}^{\infty}[e^{-(2m+1)\delta}/2m+1]^2$ and δ is a damping factor. For simplicity, the derivation for the sinusoidal case is presented here.

We attribute the change in the turn angle of bulk Er from 51°/layer at T_N to 45°/layer at T_C to magnetoelastic effects and minimize Eq. (5) with respect to $\omega_{\rm sp}$ and $\omega_{\rm CAM}$, which gives

$$\begin{aligned}\sigma^2 J^2(2\mathcal{J}_1 + 8\mathcal{J}_2 \cos\omega)\\ = -\left(\frac{K_1^{x,y}}{2}\sin^2\theta + \frac{K_2^{x,y}}{2}\cos^2\theta\right)(\epsilon_{xx}^a + \epsilon_{yy}^a)\\ -(K_1^z \sin^2\theta + K_2^z\cos^2\theta)\epsilon_{zz}^a \qquad (8)\end{aligned}$$

above T_C assuming $\omega_{\rm sp} = \omega_{\rm CAM}$ and

$$\begin{aligned}\sigma^2 J^2(2\mathcal{J}_1 + 8\mathcal{J}_2 \cos\omega_{\rm sp})\\ = -\left(\frac{K_1^{x,y}}{2}(\epsilon_{xx}^f + \epsilon_{yy}^f) + K_1^z\epsilon_{zz}^f\right), \qquad (9)\end{aligned}$$

$$\begin{aligned}\sigma^2 J^2(2\mathcal{J}_1 + 8\mathcal{J}_2 \cos\omega_{\rm CAM})\\ = -\left(\frac{K_2^{x,y}}{2}(\epsilon_{xx}^f + \epsilon_{yy}^f) + K_2^z\epsilon_{zz}^f\right), \qquad (10)\end{aligned}$$

below where f and a designate the ferromagnetic and antiferromagnetic values of the strain, respectively. We constrain the parameters to produce a cone phase at $T \le T_C$ by requiring $\cos\omega_{\rm CAM} = 1$ in Eq. (10). Equations (4) and (10) give $\mathcal{J}_1 = 3.14$ J/cm^3 and $\mathcal{J}_2 = -1.25$ J/cm^3. Using experimental parameters for bulk Er,[17,18] we can calculate the magnetoelastic coefficients by combining the equations above with the equilibrium expressions for the strains ($K_i = \sum_j c_{ij}\epsilon_{jj}$). The values of the coefficients at 20 K obtained for the squared CAM are listed in Table III.

To model the films and superlattices, the magnetoelastic energy contribution in Eq. (5) is modified to include the elastic energy contribution from the yttrium lattice

$$E_Y = \tfrac{1}{2} r_z \sum_{i,j} c_{ij}\tilde{\epsilon}_{ii}\tilde{\epsilon}_{jj}, \qquad (11)$$

where r_z is the strength of the coupling between the Er and Y and $\tilde{\epsilon}_{ii}$ are the anomalous Y strains, constrained in the basal plane to differ from the Er strains by the lattice mismatch $\epsilon_{0x,y}$. Paralleling the treatment detailed in paper I, the new energy is minimized with respect to the strains and turn angles. We obtain the following relationship for the equilibrium phase angle:

$$\cos\omega = -\frac{\mathcal{J}_1'}{4\mathcal{J}_2'}, \qquad (12)$$

where

$$\begin{aligned}\sigma^2 J^2 \mathcal{J}_1' = \sigma^2 J^2 \mathcal{J}_1 &+ \frac{1}{4\hat{c}(1+r_z)}(\hat{K}_0 + 2r_z\hat{c}\epsilon_{0x,y})\\ &\times(\hat{K}_1\sin^2\theta + \hat{K}_2 cos^2\theta)\\ &+\frac{1}{2c_{33}}K_0^z(K_1^z\sin^2\theta + K_2^z\cos^2\theta),\end{aligned}$$

(13)

TABLE III. The magnetoelastic coefficients in Eq. (6) at 20 K in units of J/cm^3. The values were extracted from the equilibrium expressions for the anomalous strains and the phase angles using strain data (Refs. 17 and 18) for bulk Er.

	$n = 0$	$n = 1$	$n = 2$
$K_n^{x,y} \equiv K_n^x + K_n^y$	−6930	58 100	−397
K_n^z	−3170	25 100	675
$\hat{K}_n$	−5360	46 000	−736

$$\begin{aligned}4\sigma^2 J^2\mathcal{J}_2' = 4\sigma^2 J^2 \mathcal{J}_2 + \frac{1}{4\hat{c}(1+r_z)}(\hat{K}_1\sin^2\theta + \hat{K}_2\cos^2\theta)^2\\ +\frac{1}{2c_{33}}(K_1^z\sin^2\theta + K_2^z\cos^2\theta)^2.\end{aligned}$$

The quantities $\hat{K}$ and $\hat{c}$ are defined

$$\hat{c} = c_{11} + c_{12} - 2\frac{c_{13}^2}{c_{33}}, \quad \hat{K} = K_x + K_y - 2\frac{c_{13}}{c_{33}}K_z. \qquad (14)$$

As suggested by the r_z dependence in Eq. (13), the value of the turn angle at a given temperature increases rapidly with lattice clamping. For a typical thin film and superlattice, the values of r_z obtained from the critical fields are 0.4 and 1.5, respectively, assuming a mismatch of 2.5%.[5] For a squared CAM at 20 K the calculated ω for the film is 54°/layer and 67°/layer for the superlattice. Although these angles are larger than those measured, this approach demonstrates how the magnetoelastic coupling can change the effective exchange constants. While the addition of anisotropy terms to Eq. (5) may alter the magnetoelastic coefficients in Table III and the resulting ω values, the overall dependence on lattice clamping would remain the same.

B. The ANNNI model

The three-plane approximation described above does not fully account for the complex features of the periodic spin order in bulk Er. Bak and Boehm[8] first suggested that the intermediate commensurate states could be explained in terms of the axial-next-nearest-neighbor Ising (ANNNI) model. Their analysis was expanded by Yokoi *et al.*[19] to include the effects of an applied field. For simplicity both considered a spin-$\frac{1}{2}$ Ising model on a simple cubic lattice with interaction $\mathcal{J}_0$ between nearest neighbors in the x-y plane. Similar to the three-plane model, the spins on neighboring planes are ferromagnetically coupled ($\mathcal{J}_1 > 0$), and the spins on next-nearest neighboring layers have an antiferromagnetic interaction ($\mathcal{J}_2 < 0$). It is assumed that $\mathcal{J}_0 = \mathcal{J}_1$. The problem was treated in the mean-field approximation, leading to the following self-consistent equations for the average spin $\langle S_j\rangle$ in layer j:

$$\begin{aligned}\langle S_j\rangle &= \tanh\left(\frac{\mathcal{H}_j}{k_B T}\right), \qquad (15)\\ \mathcal{H}_j &= 4\mathcal{J}_0\langle S_j\rangle + \mathcal{J}_1(\langle S_{j-1}\rangle + \langle S_{j+1}\rangle)\\ &+\mathcal{J}_2(\langle S_{j-2}\rangle + \langle S_{j+2}\rangle) + \mu H.\end{aligned}$$

The free energy was minimized to obtain equilibrium spin configurations at various temperatures and fields as a function of $p = -\mathcal{J}_2/\mathcal{J}_1$. The phase diagram generated by Yokoi *et al.*[19] has three distinct regions: paramagnetic, ferromagnetic, and modulated antiferromagnetic. In the modulated region the turn angle changes abruptly as a function of temperature between commensurate spin states in a manner similar to bulk Er (Fig. 1). These states are sinusoidal in the high-temperature region and develop higher-order harmonics as the temperature is decreased. In zero field the most stable of these structures[8] are the $\langle 2 \uparrow 2 \downarrow \rangle$ state (two spins up followed by two spins down) which appears above $p = 0.5$ and the $\langle 3 \uparrow 3 \downarrow \rangle$ state. The primary effect of a magnetic field[19] is to stabilize states with net moments, such as the $\langle 3 \uparrow 2 \downarrow \rangle$ state (three spins up, two spins down). In the field-dependent magnetization, transitions between commensurate states show up as steps like those observed for Er/Y superlattices (refer to Fig. 11).

We have carried out calculations based on the ANNNI model using a system of 256 layers for $J = \frac{15}{2}$. As found previously, the results represent those of bulk Er rather well for $\mathcal{J}_0 = \mathcal{J}_1$ and $p = 0.38$. We extend this treatment to the films and superlattices by including epitaxial constraints in the effective exchange parameters $\mathcal{J}_1'$ and $\mathcal{J}_2'$. Using the magnetoelastic coefficients extracted from bulk Er data, we have calculated the ratio p' from Eq. (13) for a typical film ($r_z \approx 0.4$, $\epsilon_{0x,y} = 0.025$) and superlattice ($r_z \approx 1.5$, $\epsilon_{0x,y} = 0.025$). The net effect is to move toward smaller p' as the temperature is decreased. (Due to the approximate nature of this calculation, the exact temperature dependence of p' could not be determined.)

The estimate suggests that the magnetic behavior of the Er films can be mimicked taking $p' = 0.6$, while that of the superlattice can be compared to calculations using $p' = 1.5$. Figure 13 shows the relative magnetization calculated as a function of temperature and applied field for both cases. Notice that an antiferromagnetic state persists to $T = 0$ K for low fields. The anomalies in the magnetization signify the formation of commensurate structures with phase angles that vary from 60° to 90° per layer. For example, for $p' = 0.6$ and $h = \mu H/\mathcal{J}_1' = 0.1$ the spins order in a $\langle 4 \uparrow 2 \downarrow 3 \uparrow 2 \downarrow \rangle$ up-down pattern (net moment of $\frac{3}{11}M_{\rm sat}$) near $t = 0.1$. As the temperature is increased, the spin structure jumps from the $\langle 3 \uparrow 2 \downarrow \rangle$ state to the $\langle 2 \uparrow 2 \downarrow \rangle$ configuration. The spin structure for $p' = 1.5$ and $h = 1.5$ passes through a similar series of states including $\langle 4 \uparrow 2 \downarrow 3 \uparrow 2 \downarrow \rangle$, $\langle 2 \uparrow 2 \downarrow \rangle$ and $\langle 3 \uparrow 2 \downarrow 3 \uparrow 2 \downarrow 2 \uparrow 2 \downarrow \rangle$. The spin states predicted by the ANNNI calculation are not in agreement with the configurations observed for the Er films and superlattices, but are suggestive of the general trends. A more complete treatment would require the addition of higher-order exchange terms and the effects of anisotropy.

The structural modulation of the superlattices should also be included, as was done for Gd/Fe (Ref. 20) and Ho/Y (Ref. 1) superlattices. The Ho/Y calculation suggests that the Ho layers at each Y interface, lacking second-neighbor interactions, are more ferromagnetically correlated than in bulk. This behavior is not observed for Er/Y superlattices; the phase angle data is larger than bulk values at each temperature. Evidently, the conduction electron polarization is more robust and maintains the CAM coherence at the value determined by band structure, even in the presence of intervening Y layers.

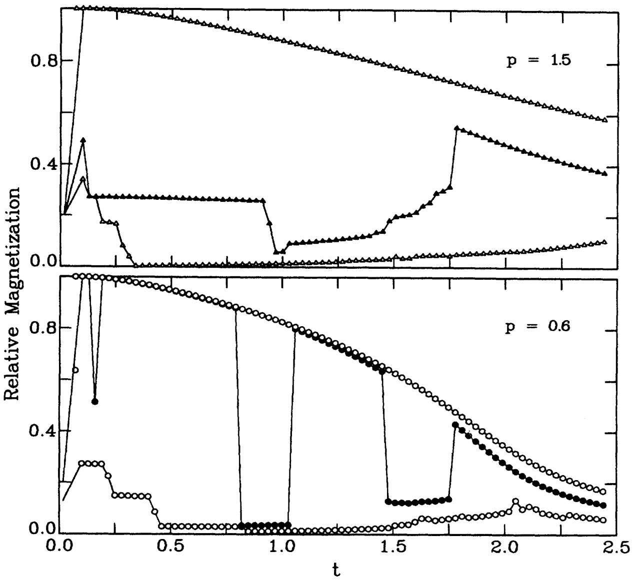

FIG. 13. Relative magnetization of the lowest energy states in the ANNNI calculation as a function of temperature for $p' = 0.6$ in reduced fields of 0.1, 0.2, and 0.3 and for $p' = 1.5$ in reduced fields of 0.5, 1.5, and 2.5. (The reduced field equals $\mu H/\mathcal{J}_1'$ and $t = k_B T/J^2\mathcal{J}_1'$.)

VII. CONCLUSION

From a comparision of the turn angle measurements with the anomalous susceptibility data, we have identified the commensurate CAM structures that develop in a series of epitaxial Er films and Er/Y superlattices. Differences in the sequence and stability of these states relative to those observed in bulk Er depend primarily on epitaxial strain. While phase angles measured for the thickest films are slightly larger than bulk values, only the high temperature "lock-in" states of the bulk develop in films thinner than 2000 Å. Phase diagrams for highly strained superlattices are dominated by the $\frac{2}{7}$ net moment state, though a new intermediate state with $\frac{1}{2}$ the saturation moment forms in high fields.

In paper I enhanced critical fields observed for these samples were explained by modifying the magnetoelastic energy to account for elastic coupling of the Er and Y lattices. By including this energy term in a phenomenological estimate of the exchange interaction, we have demonstrated here that epitaxial strain can suppress the temperature-dependence of the turn angles. We have shown how the strain effects could be incorporated into a temperature dependent ratio of the exchange coefficients, $-\mathcal{J}_2'/\mathcal{J}_1'$, in the ANNNI model, leading to additional commensurate states.

That the behavior of the films and superlattices can be approximated simply by including epitaxial constraints into the generalized Hamiltonian for bulk erbium is our principal conclusion. Strain effects clearly govern the magnetic properties in epitaxial Er systems.

ACKNOWLEDGMENTS

The work at the University of Illinois was supported through the National Science Foundation under NSF Grant Nos. DMR-85-21616 and DMR-88-20888. We are indebted to Jens Jensen and Alan Mackintosh for discussions of the peculiar nature of the exchange interaction in erbium.

---

[*] Present address: National Institute of Standards and Technology, Gaithersburg, MD 20899.

[†] Present address: Missouri University Research Reactor, University of Missouri, Columbia, MO 65211.

[1] Doon Gibbs, D.E. Moncton, K.L. D'Amico, J. Bohr, and B.H. Grier, Phys. Rev. Lett. **55**, 234 (1985).

[2] T.O. Brun, S.K. Sinha, N. Wakabayashi, G.H. Lander, L.R. Edwards, and F.H. Spedding, Phys. Rev. B **1**, 1251 (1970).

[3] Doon Gibbs, Jakob Bohr, J.D. Axe, D.E. Moncton, and K.L. D'Amico, Phys. Rev. B **34**, 8182 (1986).

[4] J. Bohr, Doon Gibbs, J.D. Axe, D.E. Moncton, K.L. D'Amico, C.F. Majkrzak, J. Kwo, M. Hong, C.L. Chien, and J. Jensen, Physica B **159**, 93 (1989).

[5] J.A. Borchers, M.B. Salamon, R.W. Erwin, J.J. Rhyne, R.R. Du, and C.P. Flynn, Phys. Rev. B **43**, 3123 (1991). This paper is referred to as paper I in the text.

[6] J.A. Borchers, Ph.D. thesis, University of Illinois, 1990.

[7] J.A. Borchers, G. Nieuwenhuys, M.B. Salamon, C.P. Flynn, R. Du, R.W. Erwin, and J.J. Rhyne, J. Phys. C **8**, 1685 (1988); R.W. Erwin, J.J. Rhyne, J.A. Borchers, M.B. Salamon, R.R. Du, and C.P. Flynn, J. Appl. Phys. **63**, 3461 (1988); J.A. Borchers, M.B. Salamon, R.R. Du, C.P. Flynn, R.W. Erwin, and J.J. Rhyne, *ibid.* **63**, 3458 (1988).

[8] Per Bak and J. von Boehm, Phys. Rev. B **21**, 5297 (1980).

[9] M. Habenschuss, C. Stassis, S.K. Sinha, H.W. Deckman, and F.H. Spedding, Phys. Rev. B **10**, 1020 (1974).

[10] W.J. Gray and R.H. Spedding, Iowa State University Report No. IS(2044), 1968 (unpublished).

[11] U. Enz, J. Appl. Phys. **32**, 22S (1961).

[12] In the sample designation $[\mathrm{Er}_n\,|\mathrm{Y}_m]_l$, n refers to the number of Er layers per bilayer, m is the number of Y layers per bilayer, and l is the total number of bilayers in the sample.

[13] R.W. Erwin, J.J. Rhyne, M.B. Salamon, J. Borchers, Shantanu Sinha, R. Du, J.E. Cunningham, and C.P. Flynn, Phys. Rev. B **35**, 6808 (1987).

[14] H.R. Child, W.C. Koehler, E.O. Wollan, and J.W. Cable, Phys. Rev. **138**, A1655 (1965).

[15] R.S. Beach, J.A. Borchers, M.B. Salamon, R. Du, and C.P. Flynn, J. Appl. Phys. **67**, 5710 (1990).

[16] Earl Callen and Herbert B. Callen, Phys. Rev. **139**, A455 (1965).

[17] M. Rosen, D. Kalir, and H. Klimker, Phys. Rev. B **8**, 4399 (1973).

[18] J.J. Rhyne and S. Legvold, Phys. Rev. **140**, A2143 (1965).

[19] C.S.O. Yokoi, M.D. Coutinho-Filho, and S.R. Salinas, Phys. Rev. B **24**, 4047 (1981).

[20] R.E. Camley, Phys. Rev. B **39**, 12 316 (1989).